Supplementary Materials for

Water Activation and Splitting by Single Metal-Atom Anions

Gaoxiang Liu,[1] Evangelos Miliordos,[2†] Sandra M. Ciborowski,[1] Martin Tschurl,[3] Ulrich Boesl,[3] Ulrich Heiz,[3] Xinxing Zhang,[4*] Sotiris Xantheas,[2,5*] and Kit Bowen[1*]

[1] Department of Chemistry, Johns Hopkins University, Baltimore, MD 21218, USA.

[2] Advanced Computing, Mathematics & Data Division, Pacific Northwest National Laboratory, Richland, WA 99354, USA

[3] Institute for Physical Chemistry, Technical University of Munich, 85748 Garching, Germany.

[4] Collaborative Innovation Center of Chemical Science and Engineering, College of Chemistry, Nankai University, Tianjin 300071, China.

[5] Department of Chemistry, University of Washington, Seattle, WA 98195, USA.

† Present address: Department of Chemistry and Biochemistry, Auburn University, Auburn, AL 36830, USA.

* Corresponding authors: kbowen@jhu.edu, sotiris.xantheas@pnnl.gov, idea.then.diligence@gmail.com

Experimental Methods

Our photoelectron spectrometer consists of one of several ion sources, a linear time-of-flight mass spectrometer, a mass gate, a momentum decelerator, a neodymium-doped yttrium aluminum garnet (Nd:YAG) laser for photodetachment, and a magnetic bottle electron energy analyzer having a resolution of 35 meV at EKE = 1 eV. Photoelectron spectra were calibrated against the well-known photoelectron spectrum of Cu^-.

The anions were generated using a laser vaporization source, ablating a rotating, translating metal rod with a pulsed Nd:YAG laser beam operating at a wavelength of 532 nm. Almost simultaneously a plume of water vapor-seeded helium gas from a pulsed gas valve (backing pressure of 100 psi) was injected directly over the rod and then allowed to flow along a 3 cm tube, where reactions and cooling occurred, before exiting into high vacuum. Negatively-charged anions were then extracted into the larger instrument prior to mass selection and photodetachment.

Experimental Results

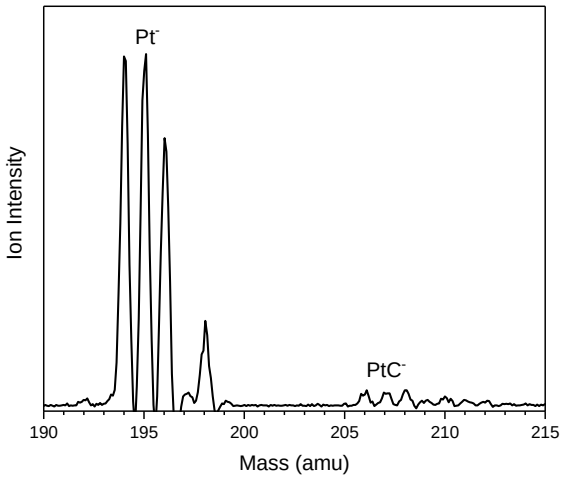

Figure S1. Mass spectrum of the anionic products formed using high vaporization laser power without water in the source.

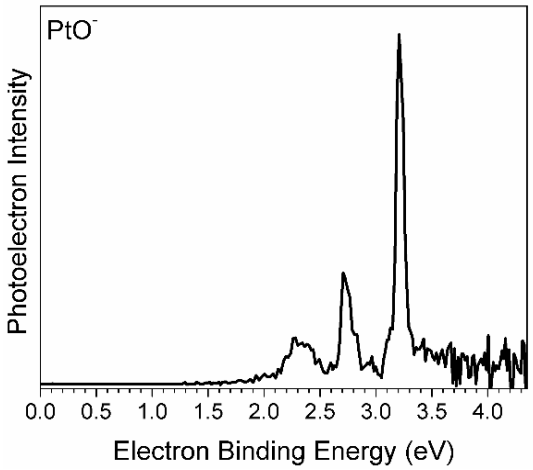

Figure S2. Anion photoelectron spectrum of PtO^- measured under the source conditions used to record the mass spectra in Figure 1 (B) and (C).

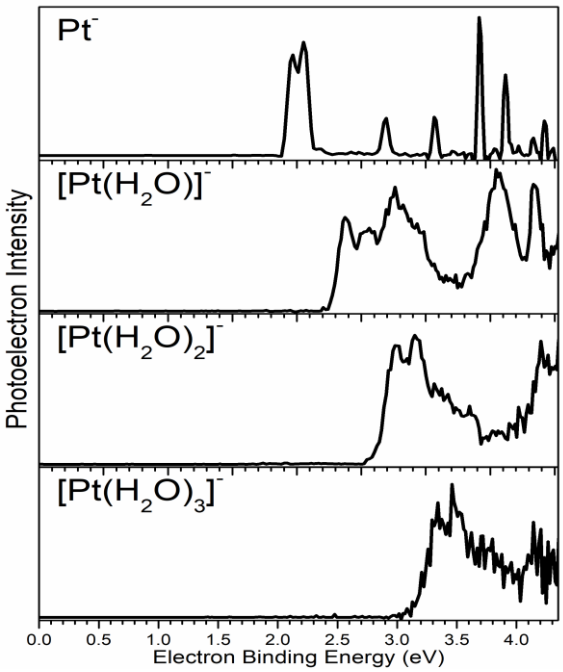

Figure S3. $[Pt(H_2O)_n]^-$ photoelectron spectra as a function of hydration number, showing that they only shift to higher EBE values and broaden after $[Pt(H_2O)_1]^-$; no new special features develop upon more hydration.

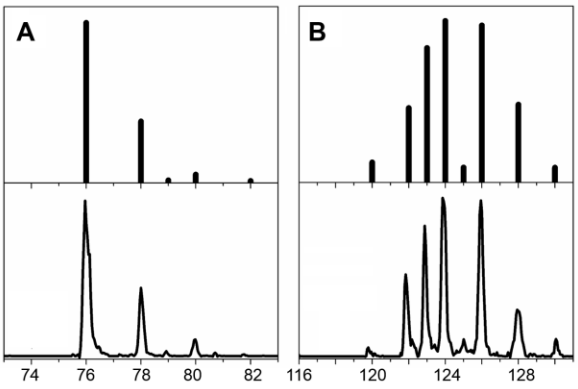

Figure S4. The top panels, A and B, present the expected isotopic mass distributions of $[M(H_2O)]^-$ species, where M = Ni and Pd, respectively. The experimental mass spectrum for each $[M(H_2O)]^-$ species is presented directly below its corresponding isotopic distributions.

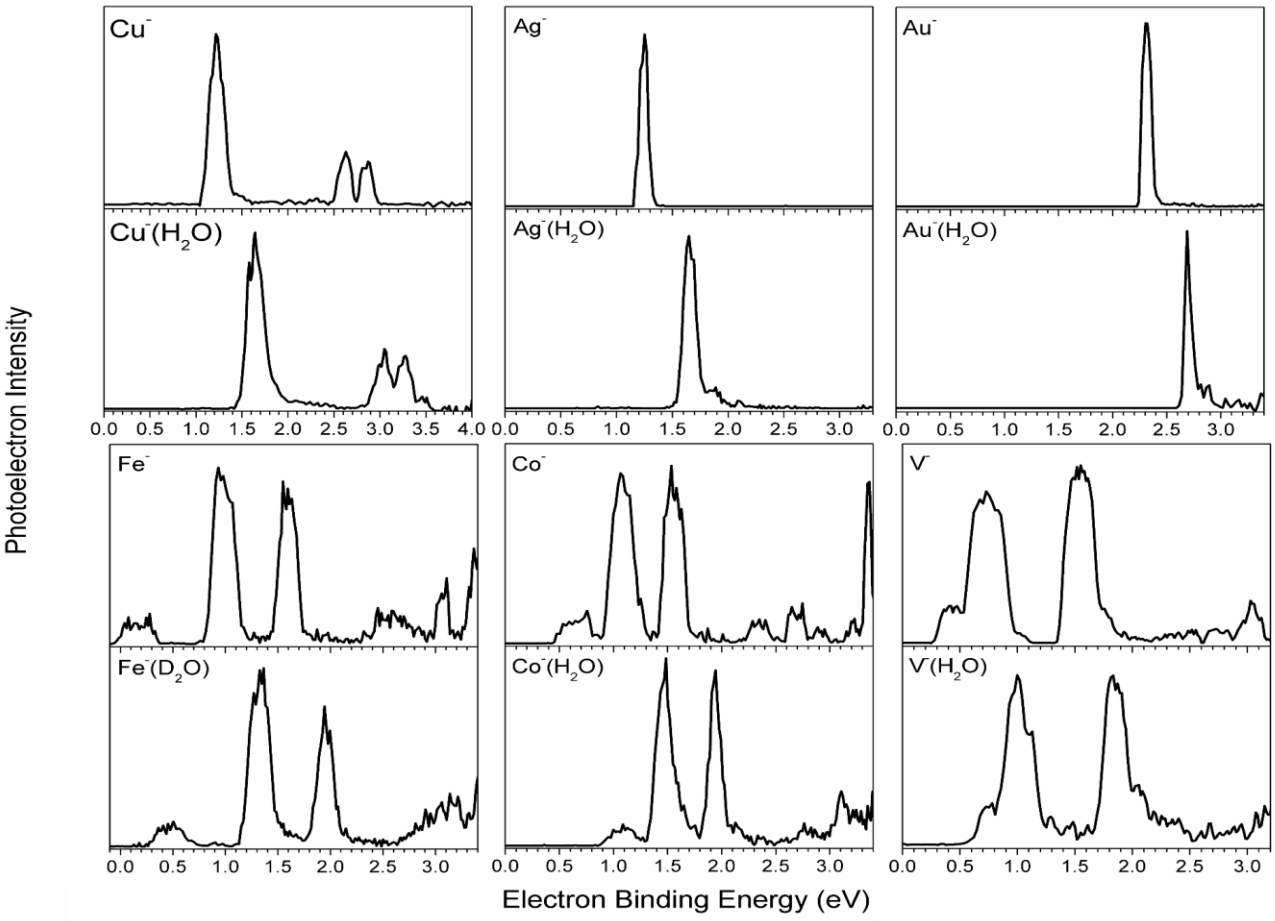

Figure S5. Anion photoelectron spectra of M^- and their corresponding $M^-(H_2O)$ solvated atomic anions, where M = Cu, Ag, Au, Fe, Co, and V.

Isotopic effects

To confirm that $HPtOH^-$ was formed from $Pt^-(H_2O)$ and not from some other process occurring in the ion source, we examined the effect of isotopic substitution (D for H), since this not only changes the mass but also depends on the barrier height shown in Figure S5. We observed that the photoelectron feature of $HPtOH^-$ is three times stronger that of $DPtOD^-$. This was due to the activation energy difference, which was in turn caused by zero-point energy differences. Upon having calculated the activation energy (with zero point energy correction), one can then use the Arrhenius equation to estimate the reaction rate. The calculation is as follows: The reaction rate constant is k; k_H is the reaction rate constant when H_2O is involved, and k_D is the reaction rate constant when D_2O is involved. Likewise, E_H is the activation energy when H_2O is involved, and E_D is the activation energy when D_2O is involved. [A] is the concentration of reactant, [B] is the concentration of product. The reaction is as follows: A → B, where A is $Pt^-(H_2O)$ or $Pt^-(D_2O)$ and B is $HPtOH^-$ or $DPtOD^-$. This is a first order reaction,

because no other reactant is involved. Then d[B]/dt = -d[A]/dt, d[A]/dt = -k[A], therefore, [A] = $[A]_0 e^{-kt}$. Since [B] = $[A]_0$ – [A], [B] = $[A]_0(1 - e^{-kt})$.

Next, we assume that the reaction times are the same for the H_2O and D_2O experiments, because the source conditions are the same. The concentrations of the reactants, [A], are also the same, because their photoelectron intensities are similar. Therefore, $[B_H]/[B_D] = (1 - e^{-kHt})/(1 - e^{-kDt})$. Based on the relative intensities of B_H and B_D in the photoelectron spectra, $[B_H]/[B_D] = 3$, so $(1 - e^{-k_H t})/(1 - e^{-k_D t}) = 3$. Using the Taylor Series, $e^x = 1 + x + x^2/2 + x^3/6\ldots$, one sees that $1 - e^{(-kt)} = kt - (kt)^2/2 + (kt)^3/6.....$ Then, by omitting the second and higher order terms, we get $1-e^{(-kt)} = kt$. Therefore, $k_H/k_D = 3$.

According to the Arrhenius Equation, $k = Ae^{-E/kT}$, where A is the total number of collisions and $e^{-E/kT}$ is the probability that any given collision will result in reaction. Hence, $k_H/k_D = e^{(E_D-E_H)/kT}$, where E_H and E_D are the activation energies, *k* is the Boltzmann constant and T is the reaction temperature. Our ZPE-corrected CCSD(T)/aug-cc-pVTZ calculations find that E_D = 1.080 eV and E_H = 1.011 eV (see Table **S8**). Therefore, $k_H/k_D = e^{800/T}$.

Thus, we have $k_H/k_D = 3$ and $k_H/k_D = e^{800/T}$. Therefore, using this set of values the reaction temperature, T, is implied to be 728 K. From the Arrhenius equation, $e^{-E/kT}$ is the probability that any given collision will result in reaction. Thus, using T = 728 K and E_H = 0.768 eV, $e^{-E_H/kT}$ is 4.88×10^{-6} for the H_2O case. Using T = 728 K and E_D = 0.837 eV, $e^{-ED/kT}$ is 1.63×10^{-6} for the D_2O case. Here, the total collision number, A, is the number of $Pt(H_2O)^-$ or $Pt(D_2O)^-$ clusters, since this is an unimolecular reaction; A is of the order of 10^9-10^{13} per laser shot. While this number can easily vary with different source conditions, the probability, $e^{-E/kT}$, is a more pertinent parameter. It is the rate at which $Pt(H_2O)^-$ or $Pt(D_2O)^-$ become $HPtOH^-$ or $DPtOD^-$, respectively.

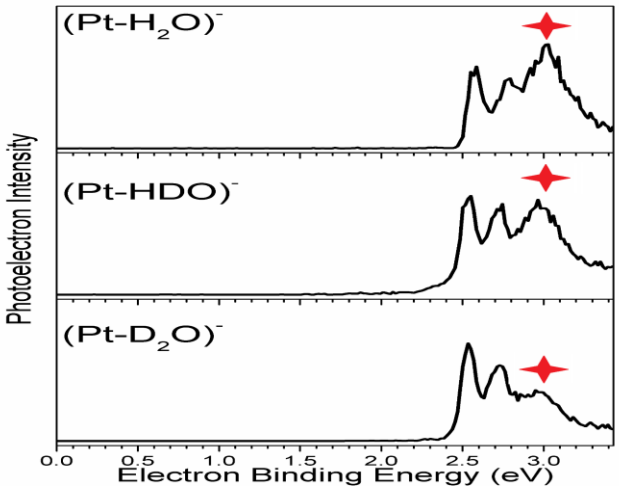

Figure S6. Photoelectron spectra of $(Pt\text{-}H_2O)^-$, $(Pt\text{-}HDO)^-$, and $(Pt\text{-}D_2O)^-$, showing effects of isotopic substitution. Red stars mark the peak locations of the $HPtOH^-$, $HPtOD^-$, and $DPtOD^-$ isomers.

Theoretical methods

The calculations were performed at the Coupled Cluster Singles and Doubles with perturbatively connected Triples [CCSD(T)] based on a Restricted Hartree-Fock (RHF) wavefunction and the internally contracted Multi-Reference Configuration Interaction (*ic*MRCI) levels of theory *(1, 2)*. CCSD(T) was used only for the cases where the wavefunction is of considerable single reference nature, as validated via Complete Active Space Self Consistent Field (CASSCF) calculations. The *ic*MRCI methodology, applied for the $M^{0,-}(H_2O)$ molecular systems, was based on a Multi-Configuration Self-Consistent Field (MCSCF) reference function where the valence *s* and *d* electrons of the metal (4*s*, 3*d* for Ni, 5*s*, 4*d* for Pd, 6*s*, 5*d* for Pt) were allocated into the *ns*, (*n*-1)*d* and *np* valence orbitals (*n* = 4, 5, 6 for Ni, Pd, and Pt, respectively). We used the family of augmented correlation-consistent basis sets of Dunning and coworkers (aug-cc-pVXZ, X = T, 5) *(3, 4)*. For the Pd and Pt metals, the 28 and 60 inner electrons were represented by the corresponding Stuttgart relativistic pseudopotentials (aug-cc-pV*n*Z-PP basis sets) *(5, 6)*. The relativistic effects for Ni were taken into account through the fourth order Douglas-Kroll-Hess (DKH4) approximation *(7-9)* using the more suitable aug-cc-pV*n*Z-DK basis sets for the Ni atom. For simplicity, the basis sets will be denoted as AXZ for all three metals implying the PP or DK notation. Finally, the 1*s* electrons of oxygen, the 18 (1*s* through 3*p*) electrons for Ni, and the 4 electrons for Pd (4*s*, 4*p*) and Pt (5*s*, 5*p*) were kept doubly occupied when computing the non-dynamic electron correlation. All calculations were performed with MOLPRO *(10)*.

We first discuss the photoelectron spectra (PES) of the naked metals. The ground states of Ni^-, Pd^-, and Pt^- are ^2D ($4s^23d^9$), ^2S ($5s^14d^{10}$), and ^2D ($6s^25d^9$), respectively *(1, 2)*. The $^2D_{5/2}$ ($5s^24d^9$) state of Pd^- lies just 0.14 eV higher than ^2S, while the ^2S state for Ni^- and Pt^- lie experimentally at least 1 eV above the corresponding $^2D_{5/2}$ ground state *(1, 2)*. Based on the assignments provided by Peppernick et al *(13)* the lowest energy bands of the PES observed for Pd and Pt are due to the ($^2D_{5/2}$,$^2S_{1/2}$) → $^1S_0$ and $^2D_{5/2}$ → ($^3D_{2,3}$,$^3F_4$) transitions, respectively. For the case of Ni, the present experimental spectra have a different shape from those of ref. *3* (which were obtained at the same photon energy of 532 nm). Specifically, these authors report a single band ($^2D_{5/2}$ → $^3D_3$) in the region of 1.1 eV and do not assign any peak to the $^2D_{5/2}$ → $^3F_4$ transition, which corresponds to the one between the respective ground states of the anionic and the neutral nickel atoms. In contrast, the present spectrum shows a double peak in this region.

Our results are tabulated in Tables **S1, S2, S3**. All of the high spin states have been examined at both the CCSD(T)/ATZ and CCSD(T)/A5Z levels of theory. The differences due to the basis set (i.e. between ATZ and A5Z) are in all cases < 0.1 eV and therefore the use of the ATZ basis set for the hydrated complexes should be considered as a good compromise between feasibility and accuracy.

The ground state of the Ni^- and Pt^- ions is ^2D of the s^2d^9 nature, whereas that of Pd^- is a ^2S state of s^1d^{10} character. The calculated electron affinities (EA), albeit stripped of the spin-orbit coupling effects, are in good agreement with the experimental values. Namely, the calculated CCSD(T)/ATZ (vs. the experimental *(11, 12)*) values are 1.11 (1.157), 0.44 (0.562), and 2.01 (2.125) eV for the Ni, Pd, and Pt metals, respectively. The corresponding *ic*MRCI(+Q) EAs are 0.39 (0.71), 0.07 (0.19), and 1.78 (1.89) eV. Note that the *ic*MRCI values fall considerably short in providing accurate EA values. The *ic*MRCI+Q result tends to recover some of the missing

correlation energy by approximately including the contribution of higher-than-double excitations through the Davidson correction. On the other hand, the CCSD(T) results are closer to experiment and for this reason the *ic*MRCI+Q energies (E_{MRCI+Q}) will be from now on used to estimate the energy for only the states with reference character that cannot be described by a single determinant. For example, the energy difference (ΔE) between the Ni (^{1}D) (open singlet) and the Ni^- (^{2}D; $4s^2 3d^9$) states is estimated via the difference between the ^{1}D and ^{3}D states of Ni as:

$$\Delta E[\mathrm{Ni}(^1\mathrm{D}) \leftarrow \mathrm{Ni}^-(^2\mathrm{D})] = \Delta E_{CCSD(T)}[\mathrm{Ni}(^3\mathrm{D}) \leftarrow \mathrm{Ni}^-(^2\mathrm{D})] + \{E_{MRCI+Q}[\mathrm{Ni}(^1\mathrm{D})] - E_{MRCI+Q}[\mathrm{Ni}(^3\mathrm{D})]\}. \quad (1)$$

We now consider the singly hydrated species. Initially, the ground states of the $M^-(H_2O)$ anions were optimized at the CCSD(T)/aug-cc-pVTZ level of theory. The CCSD(T)/ATZ optimal geometry for the ground state $M^-(H_2O)$, which is typical for all three metals M, is shown in Figure **S7(a)**. The geometrical parameters for all metal ion monohydrate optimal structures are listed in Table **S4**. Interestingly, the metal-oxygen distance is the largest for Ni (3.336 Å) and the shortest for Pd (3.150 Å), while the Pt-O distance lies somewhere in-between (3.315 Å). In all cases the water molecule is oriented so that one of its hydrogen atoms is directed towards the metal center, a typical arrangement of a charge – dipole interaction. The M···H-O angle varies from 156^0 - 164^0. The free OH bond lengths are in the range 0.963 - 0.964 Å, while the hydrogen-bonded one ranges from 0.981 - 0.991 Å, being elongated by 0.02-0.03 Å with respect to the free OH due to the interaction with the negative charge. The water HOH angle is ~100^0 for all singly hydrated anionic clusters. Compared to the free water molecule at the same level of theory, the HOH angle has decreased by ~4 degrees, while the free OH bond length remains practically intact.

Using the CCSD(T)/ATZ optimal geometries of the anionic systems, we calculated the vertical excitation energies to the same electronic states as the ones studied for the pure metal. Note, however, that now the degeneracy of the electronic states due to the spherical symmetry of the atom is lifted due to the "symmetry-breaking" effect caused by the presence of the water molecule. For example, the atomic D states will split into 5 (three A′ and two A′′ states under C_s symmetry) whereas the atomic F states into 7 (three A′ and four A′′ states under C_s symmetry) components. The energy of all of these components is calculated at the *ic*MRCI and *ic*MRCI+Q levels, while only that of the lowest component for each manifold is calculated at the CCSD(T) level, denoted as *E*[CCSD(T)/ATZ]. In Tables **S1, S2, and S3** we list the average energy of all of these components under the *ic*MRCI(+Q)/ATZ columns. We take into account, however, the distribution of the energies at the *ic*MRCI+Q level, δE[*ic*MRCI+Q], in the final CCSD(T)/ATZ energy differences from the ground state of $M^-(H_2O)$ [ΔE values] :

$$E[\mathrm{CCSD(T)/ATZ}] - E_0[\mathrm{CCSD(T)/ATZ}] < \Delta E < E[\mathrm{CCSD(T)/ATZ}] - E_0[\mathrm{CCSD(T)/ATZ}] + \delta E[ic\mathrm{MRCI+Q}], \quad (2)$$

where E_0[CCSD(T)/ATZ] is the energy of the ground state of $M^-(H_2O)$. It should be mentioned that a further dispersion and/or shift in the energies is expected to occur after considering the spin-orbit effects, especially for Pt. As a result, the use of the atomic electronic terms for the hydrated clusters is only nominal.

For reasons of completeness, we also obtained the optimal geometries for the lowest energy components of the ^{3}D and ^{3}F states for the neutral $M(H_2O)$ systems, M = Ni, Pt, and the only component of the ^{1}S state of $Pd(H_2O)$. These structures along with their absolute energies are given in Table **S4**. The Ni-O and Pt-O distances for both the ^{3}D and ^{3}F states are appreciably

longer compared to the ground ^{2}D state of the corresponding anionic systems by more than 0.15 Å and 0.5 Å for ^{3}D and ^{3}F, respectively. However, the Pd-O length actually decreases going from $Pd^-(^2S;\ 5s^1 4d^{10})$ to $Pd(^1S;\ 4d^{10})$ by 0.02 Å. The reason may be the absence of the diffuse 5*s* electrons in the case of Pd(^{1}S).

The results listed in Tables **S1, S2, and S3** for the hydrated species indicate larger energy differences (compared to those for the single metals) between the anionic and neutral species, thus increasing the electron affinity by more than 0.5 eV in many cases. This is in agreement with the fact that the negatively charged metal anions are stabilized more by water than their neutral counterparts. The comparison between the photoelectron spectra of the bare metals and the singly hydrated ones confirms this reasoning.

As discussed in the manuscript, the spectra of hydrated metal anions reveal additional bands which are not simply those of the naked metals shifted to higher electron detachment energies. In an attempt to explain the observed spectral features, we investigated the existence of other isomers of the hydrated species with the MOH_2 stoichiometry, M = Ni, Pd, Pt. Our calculations suggested that the $HMOH^-$ isomers are more stable than the $M^-(H_2O)$ ones, with energy barriers between the two minima of the order of ~1 eV. Figures. **S7(b)** and **S7(c)** depict the typical geometrical structures for the $HMOH^-$ and the transition states connecting the $HMOH^-$ and $M^-(H_2O)$ minima, while Table **S5** lists the different bond lengths and angles for M = Ni, Pd, Pt.

We calculated the vertical excitation energies from the $HMOH^-$ (^{2}A state) isomer to the lowest singlet (^{1}A) and triplet states (^{3}A) of neutral HMOH. In Table **S6** we tabulate the optimal geometries of all these states together with their equilibrium energy and their energy at the $HMOH^-$ geometry. The latter is used to calculate the required vertical excitation energies. The ^{1}A states are of closed electronic shell nature, whereas the two lone electrons of the ^{3}A states are localized on the metal. In both cases the single reference character was confirmed by tentative MCSCF calculations, further validating the use of the CCSD(T) method (see Table **S12**). Observe that for HMOH the ^{1}A state is favored over the ^{3}A one in the case of M = Ni, but the singlet state is lower than the triplet in the case of M = Pd, Pt. To rationalize this behavior we see HMOH as $H^-M^{2+}OH^-$ and we calculated the ^{3}F-^{1}D gap for the in situ M^{2+} at MRCI. We found that the singlet-triplet gap is 15099, 11280, and 9317 cm^{-1} for M = Ni, Pd, and Pt, respectively. The trend shows clearly that the singlet state is stabilized further going from Ni to Pd and Pt.

In Figure **S7(a)-(c)**, H_f denotes the "free" H atom of the OH group, H_b the "hydrogen bonded" H atoms in the $M^-(H_2O)$ minima [Figure **S7(a)**] and the "covalently bonded" one in the transition state [Figure **S7(c)**], whereas H_a is used for the H atom of the M-H bond [Figure **S7(b)**] in the $HMOH^-$ minimum [reverting to H_b at the transition state, Figure **S7(c)**]. Notice that the triplet states have consistently longer H_a-M and M-O bonds, whereas the O-H_f length remains intact. The location of the H_a atom is quite different in the two spin multiplicities, as indicated by the different ϕ(H_a-M-O) angles and the δ(H_a-M-O-H_f) dihedral angles (see Table **S6**). The H_a-M and M-O bonds further elongate in the case of the $HMOH^-$ (^{2}A) state, where a different set of ϕ(H_a-M-O) and δ(H_a-M-O-H_f) angles is obtained for that state (see Table **S5**).

The difference between the equilibrium energy (E_e) of the HMOH minimum and its energy at the $HMOH^-$ (^{2}A) optimal geometry (E_{vert}) is considerably larger for the ^{1}A state (30-40 mE_h) than for the ^{3}A one (~3 mE_h) for all three metals (see Table **S6**). This suggests that the

geometry of the ^{3}A state of HMOH is closer to that of the ^{2}A state of $HMOH^-$, compared to the corresponding one for the ^{1}A state. Indeed, the root-mean-square-deviation (RMSD) between the HMOH (^{3}A) and $HMOH^-$ (^{2}A) geometries is approximately seven times smaller than the corresponding RMSD value between the HMOH (^{1}A) and $HMOH^-$ (^{2}A) geometries. The RMSD is calculated as

$$\mathrm{RSMD} = \sqrt{\frac{\sum_{i=1}^{N}(\vec{r}_i^{(1)} - \vec{r}_i^{(2)})^2}{N}}$$

and it is minimized as described in ref. *4*. *N* is the number of atoms (*N* = 4) and $\vec{r}_i^{(k)}$ is the position vector of the i^{th} atom of the k^{th} molecule. Namely, RMSD(^{1}A – ^{2}A) = 0.57, 0.52, 0.46 Å and RMSD(^{3}A – ^{2}A) = 0.08, 0.06, 0.07 Å for M = Ni, Pd, Pt, respectively.

Figure **S8, S9** and **S10** summarize our results for the vertical excitation energy from the optimal geometry of the ground state of $M^-(H_2O)$ and $HMOH^-$ to the several electronic states of the neutral species. In the case of $M(H_2O)$ the energy of the most stable component for each "atomic" electronic term was selected (see Tables **S1**, **S2** and **S3**). These Figures also show the relative energetics for the two isomers of the negatively charged species, as well as their inter-conversion barrier. In the case of HPtOH we computed the vertical energy of a second ^{3}A state (2^3A) not included in Table **S6**. The two unpaired electrons in 2^3A state are also located on the metal center but they occupy different 5*d* orbitals. Based on the vertical excitation energy values shown in Figures. **S8, S9** and **S10**, we are able to assign the additional bands in the PES spectra of the hydrated metal species (see manuscript).

The isotopic effect observed for Pt-water cluster can be attributed to the dangling hydrogen H_a [see Figure **S7(b)**]. Recall that the position of H_a with respect to the remaining molecular frame is generally different between the anionic and neutral species; compare also the values for $R(H_aM)$, $\varphi(H_aMO)$, and $\delta(H_aMOH_f)$ between Tables **S5** and **S6**. Therefore, the transition from $HMOH^-$ to HMOH is likely to involve not only ground but also excited vibrational levels to obtain considerable overlap of the vibrational wavefunctions between the anions and the neutrals (Franck-Condon factor). The replacement of H_a with deuterium reshuffles the position of the involved excited vibrational levels and thus alters the maxima of the corresponding vibrational wavefunctions. This, in turn, can increase or decrease the overlap between the (ground) vibrational level of $HMOH^-$ with the (excited) vibrational levels of HMOH changing the Franck-Condon factor and finally affecting the band intensities.

Table 7 lists the vibrational frequencies for the $M(X_2O)^-$, $XMOX^-$ structures, and the transition state connecting them with X = H or D. Table 8 shows how the $M(X_2O)^- \rightarrow XMOX^-$ activation barrier is affected by zero-point energy (ZPE) and spin-orbit (SO) corrections for both hydrogen and deuterium.

Next, we performed CCSD(T)/ATZ calculations to study the dehydrogenation reaction of $HMOH^-$ leading to the $H_2 + MO^-$ products on the lowest potential energy surface of doublet spin multiplicity. We found that initially the hydrogen of the hydroxyl group migrates to the metal end (forming H_2MO^-) via a transition state TS_1 where the migrating hydrogen is shared between the metal and the oxygen. Typical structures for H_2MO^- and TS_1, both of which are planar, are shown in Figure **S11**.

The optimal geometries and absolute energies of these structures are listed in Table **S9**. The lone electron is localized on the metal center at the TS_1 geometry but on the oxygen atom at the H_2MO^- minimum. In both cases this electron occupies an out-of-plane molecular orbital ($^2A''$ state). The $R(H_1\text{-}H_2)$ distance in the H_2MO^- minimum for M = Ni, Pd, and Pt is 1.642, 0.951, 1.614 Å, respectively. The two hydrogen atoms in the Ni and Pt compounds are clearly dissociated forming a single bond with the metal center. On the other hand, there is a bonding interaction between the two hydrogen atoms in the case of Pd, resulting in a structure with a nearly equilateral $H_1\text{-Pd-}H_2$ triangle.

The energy barrier for $HMOH^- \rightarrow H_2MO$ is 1.97, 2.14, and 1.84 eV for M = Ni, Pd, and Pt, which is practically twice as large than the one for $M^-(H_2O) \rightarrow HMOH^-$ [1.22, 1.05, and 1.01 eV for M = Ni, Pd, and Pt]. The H_2PtO^- minimum is considerably more stable than the H_2PdO^- and H_2NiO^- ones. The last minimum (H_2NiO^-) is quite shallow since the barrier to convert to the $HNiOH^-$ minimum is just 0.15 eV. Finally, the dehydrogenation process from H_2MO^- to H_2 + MO^- is barrierless and endothermic in all three cases. The energy required to detach H_2 from the H_2MO^- minimum is 1.00, 1.39, and 1.89 eV for M = Ni, Pd, and Pt, respectively. Finally, we calculated the vertical excitation energies from the ground state of H_2MO^- to the ground and first excited states of its neutral counterpart. The absolute (E_e) and excitation (E_{vert}) energies (in eV) are listed in Table **S10**.

Finally, we calculated the spin-orbit (SO) splittings for all of the studied structures. Our final results for the ground state potential energy landscape including ZPE and SO corrections are listed in Table **S11**.

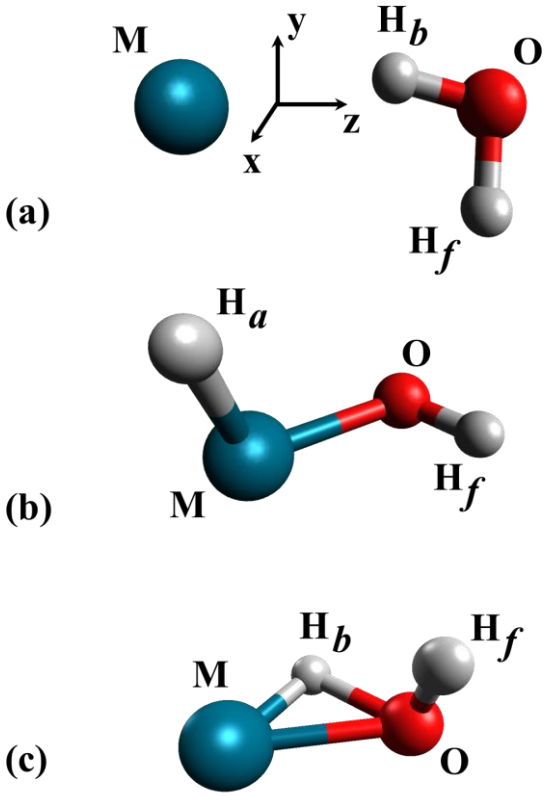

Figure S7. Typical optimal geometries for: (a) the $M^{0,-}(H_2O)$ minima, (b) the $HMOH^{0,-}$ minima, and (c) the transition states between them.

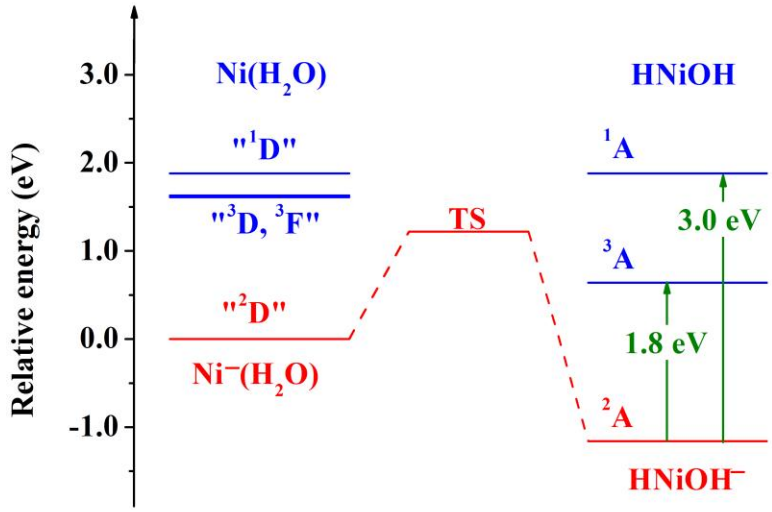

Figure S8. Energy level diagram for the $Ni^{0,-}(H_2O)$ and $HNiOH^{0,-}$ clusters at CCSD(T)/ATZ. Red and blue colors correspond to the negatively charged and neutral species, respectively. TS denotes the transition state between the two anionic isomers.

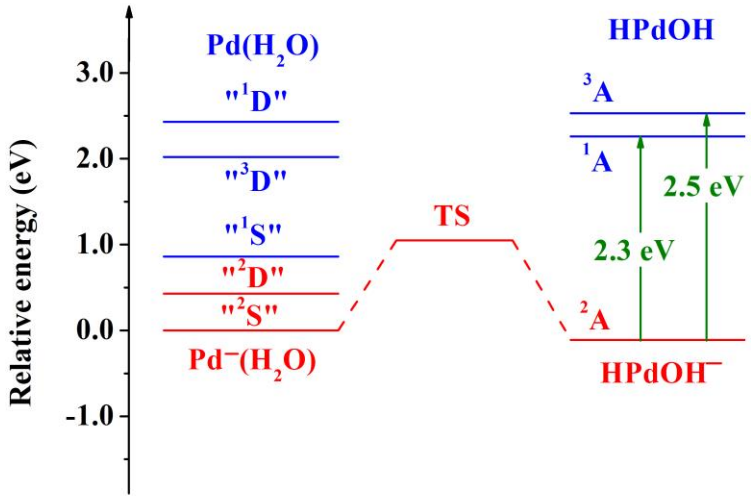

Figure S9. Same as Figure S8 but for the $Pd^{0,-}(H_2O)$ and $HPdOH^{0,-}$ species.

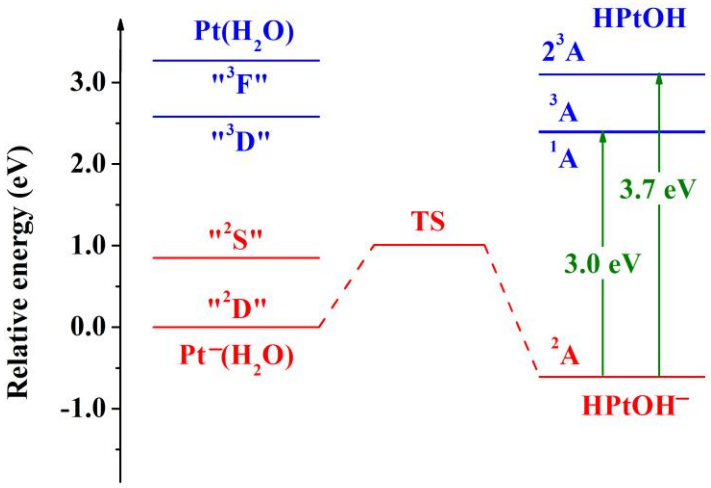

Figure S10. Same as Figure S8 and S9 but for the $Pt^{0,-}(H_2O)$ and $HPtOH^{0,-}$ species.

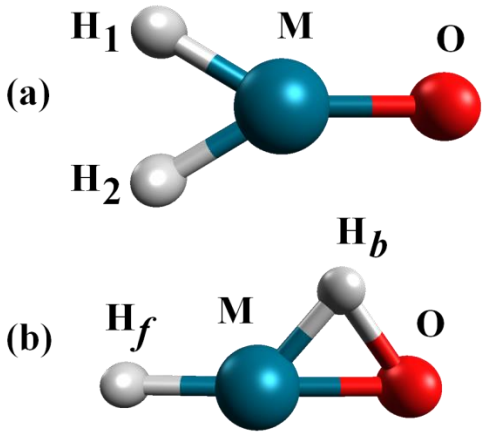

Figure S11. Typical optimal geometries for: (a) the $H_2MO^{0,-}$ minima, and (b) the transition states between them and $HMOH^{0,-}$.

Table S1. DKH4-*ic*MRCI, DKH4-*ic*MRCI+Q, and DKH4-CCSD(T) absolute energies (a.u.) and relative shifts (ΔE in eV) of the $Ni(H_2O)_{n=0-1}$ and $Ni^-(H_2O)_{n=0-1}$ species with the aug-cc-pVTZ-DK (ATZ) and aug-cc-pV5Z-DK (A5Z) basis sets.

Species [a]	*ic*MRCI/ATZ[b]	*ic*MRCI+Q/ATZ[b]	CCSD(T)/ATZ[c]	CCSD(T)/A5Z	ΔE/ATZ[d,e]	ΔE/A5Z[d]
			Ni			
Ni^- (^{2}D; s^2d^9)	-1519.460745	-1519.486402	-1519.505897	-1519.544905	0.000	0.000
Ni (^{3}F; s^2d^8)	-1519.446297	-1519.460305	-1519.464988	-1519.499220	1.113	1.243
Ni (^{3}D; s^1d^9)	-1519.420455	-1519.453258	-1519.464724	-1519.502321	1.120	1.159
Ni (^{1}D; s^1d^9)	-1519.418196	-1519.439669			1.490 [f]	1.529 [f]
Ni^- (^{2}S; s^1d^{10})			-1519.422158	-1519.466506	2.279	2.133
			$Ni(H_2O)$			
Ni^- (^{2}D)	-1595.812195	-1595.877752	-1595.913763		0.000-0.068	
Ni ("^{3}F")	-1595.795702	-1595.843514	-1595.854027		1.625-1.640	
Ni ("^{3}D")	-1595.784197	-1595.836338	-1595.856638		1.554-1.667	
Ni ("^{1}D")	-1595.772437	-1595.825487			1.850-1.939 [f]	
Ni^- ("^{2}S")			-1595.832373		2.215	

[a] The *in situ* atomic state of Ni and Ni^- is listed in quotes for the hydrated species.

[b] The average energy of the components for each state is reported for the hydrated species.

[c] The energy of the lowest lying component for each state is reported for the hydrated species.

[d] Relative energy with respect to Ni^- (^{2}D) at the CCSD(T)/AXZ level (X = T, 5).

[e] The energy range, spanned by the components of each state at the *ic*MRCI+Q level, has been added to ΔE via see Eq. (2) for the hydrated species.

[f] ΔE[Ni (^{1}D)] = ΔE[Ni (^{3}D)] + E[Ni (^{1}D); *ic*MRCI+Q/ATZ] – E[Ni (^{3}D); *ic*MRCI+Q/ATZ].

Table S2. *ic*MRCI, *ic*MRCI+Q, and CCSD(T) absolute energies (a.u.) and relative shifts (ΔE in eV) for the $Pd(H_2O)_{n=0-1}$ and $Pd^-(H_2O)_{n=0-1}$ species with the aug-cc-pVTZ-PP (ATZ) and aug-cc-pV5Z-PP (A5Z) basis sets.

Species [a]	*ic*MRCI/ATZ [b]	*ic*MRCI+Q/ATZ[b]	CCSD(T)/ATZ [c]	CCSD(T)/A5Z	ΔE/ATZ [d,e]	ΔE/A5Z [d]
			Pd			
Pd^- (^2S; s^1d^{10})	-126.939646	-126.967311	-126.991696	-127.0328960	0.000	0.000
Pd^- (^2D; s^2d^9)	-126.945690	-126.968959	-126.981152	-127.0197622	0.287	0.357
Pd (^1S; d^{10})	-126.937054	-126.960285	-126.975477	-127.0152941	0.441	0.479
Pd (^3D; s^1d^9)	-126.911157	-126.929768	-126.938742	-126.9760446	1.441	1.547
Pd (^1D; s^1d^9)	-126.897665	-126.917032			1.788 [f]	1.894 [f]
			$Pd(H_2O)$			
Pd^- ("^2S")	-203.230621	-203.312222	-203.352566		0.000	
Pd^- ("^2D")	-203.249423	-203.312129	-203.338437		0.384-0.489	
Pd ("^1S")	-203.228505	-203.292716	-203.320969		0.860	
Pd ("^3D")	-203.206063	-203.260186	-203.280413		1.963-2.092	
Pd ("^1D")	-203.192759	-203.249368			2.258-2.603 [f]	

[a] The *in situ* atomic state of Pd and Pd^- is listed in quotes for the hydrated species.

[b] The average energy of the components for each state is reported for the hydrated species.

[c] The energy of the lowest lying component for each state is reported for the hydrated species.

[d] Relative energy with respect to Pd^- (^2S) at the CCSD(T)/AXZ level (X = T, 5).

[e] The energy range, spanned by the components of each state at the *ic*MRCI+Q level, has been added to ΔE via see Eq. (2) for the hydrated species.

[f] ΔE[Pd (^1D)] = ΔE[Pd (^3D)] + E[Pd (^1D); *ic*MRCI+Q/ATZ] – E[Pd (^3D); *ic*MRCI+Q/ATZ].

Table S3. *ic*MRCI, *ic*MRCI+Q, and CCSD(T) absolute energies (a.u.) and relative shifts (ΔE in eV) of the $Pt(H_2O)_{n=0-1}$ and $Pt^-(H_2O)_{n=0-1}$ species with the aug-cc-pVTZ-PP (ATZ) and aug-cc-pV5Z-PP (A5Z) basis sets.

Species [a]	*ic*MRCI/ATZ [b]	*ic*MRCI+Q/ATZ [b]	CCSD(T)/ATZ [c]	CCSD(T)/A5Z	ΔE/ATZ [d,e]	ΔE/A5Z [d]
			Pt			
Pt^- (^{2}D; s^2d^9)	-118.8713184	-118.8966609	-118.9080651	-118.9410143	0.000	0.000
Pt^- (^{2}S; s^1d^{10})	-118.8212070	-118.8544021	-118.8791173	-118.9140676	0.788	0.733
Pt (^{3}D; s^1d^9)	-118.8059743	-118.8270445	-118.8341751	-118.8653361	2.011	2.059
Pt (^{3}F; s^2d^8)	-118.7925288	-118.8098709	-118.8163462	-118.8450933	2.496	2.610
			$Pt(H_2O)$			
Pt^- (“^{2}D”)	-195.177516	-195.242935	-195.271215		0.000-0.148	
Pt^- (“^{2}S”)	-195.133755	-195.211850			0.846 [f]	
Pt (“^{3}D”)	-195.097759	-195.156960	-195.179029		2.509-2.652	
Pt (“^{3}F”)	-195.085892	-195.139068	-195.151803		3.249-3.289	

[a] The *in situ* atomic state of Ni and Ni^- is listed in quotes for the hydrated species.

[b] The average energy of the components for each state is reported for the hydrated species.

[c] The energy of the lowest lying component for each state is reported for the hydrated species.

[d] Relative energy with respect to Pt^- (^{2}S) at the CCSD(T)/AXZ level (X = T, 5).

[e] The energy range, spanned by the components of each state at the *ic*MRCI+Q level, has been added to ΔE via see Eq. (2) for the hydrated species.

[f] $\Delta E[Pt^-(^2S)] = \Delta E[Pt^-(^2D)] + E[Pt^-(^2S); icMRCI+Q/ATZ] - E[Pt^-(^2D); icMRCI+Q/ATZ]$.

Table S4. Optimal geometries (distances in Å, angles in degrees, see Figure S7(a)) and equilibrium energies E_e (in a.u.) of the ground electronic state of $M^-(H_2O)$, M = Ni, Pd, Pt, and the ground and first excited state of its neutral counterpart at the CCSD(T)/ATZ level of theory.

	$Ni^-(^2D; 4s^23d^9)$ [a]	**$Pd^-(^2S; 5s^14d^{10})$**	**$Pt^-(^2D; 6s^25d^9)$** [a]
R(MO)	3.336	3.150	3.315
$R(OH_b)$ [b]	0.981	0.991	0.989
$R(OH_f)$ [c]	0.963	0.964	0.963
$\varphi(MOH_f)$ [c]	82.6	84.9	88.8
φ(HOH)	99.9	100.0	100.2
E_e	-1595.913764	-203.352567	-195.271214
	Ni ($^3D; 4s^13d^9$) [d]	**Pd ($^1S; 4d^{10}$)**	**Pt ($^3D; 6s^15d^9$)** [d]
R(MO)	3.511	3.130	3.481
$R(OH_b)$ [b]	0.966	0.974	0.968
$R(OH_f)$ [c]	0.962	0.963	0.962
$\varphi(MOH_f)$ [c]	105	98.7	106.3
φ(HOH)	103.9	103.8	104.0
E_e	-1595.857498	-203.321649	-195.180056
	Ni ($^3F; 4s^23d^8$) [e]		**Pt ($^3F; 6s^25d^8$)** [e]
R(MO)	3.997		3.845
$R(OH_b)$ [b]	0.963		0.964
$R(OH_f)$ [c]	0.962		0.962
$\varphi(MOH_f)$ [c]	103.7		105.7
φ(HOH)	104.0		104.1
E_e	-1595.856811		-195.155105

[a] The $s^2 d_{z^2}^2 d_{xz}^2 d_{yz}^2 d_{x^2-y^2}^2 d_{xy}^1$ ($^2A''$ under the C_s point group) component is considered.

[b] H_b denotes the hydrogen atom directed to the metal (see Figure S1(a)).

[c] H_f denotes the free hydrogen atom of the OH group (see Figure S1(a)).

[d] The $s^1 d_{z^2}^2 d_{xz}^2 d_{yz}^2 d_{x^2-y^2}^2 d_{xy}^1$ ($^3A''$ under the C_s point group) component is considered.

[e] The $s^2 d_{z^2}^2 d_{yz}^2 d_{x^2-y^2}^2 d_{xz}^1 d_{xy}^1$ ($^3A'$ under the C_s point group) component is considered.

Table S5. Optimal geometries (distances in Å, angles in degrees) and equilibrium energies E_e (in a.u.) of the ground electronic state (^{2}A) of $HMOH^-$ and its transition state (TS) to the $M^-(H_2O)$ minimum, M = Ni, Pd, Pt, at the CCSD(T)/ATZ level of theory. The atomic notation is given in Figures S7(b) and (c).

	$HNiOH^-$	**$HPdOH^-$**	**$HPtOH^-$**
$R(H_aM)$	1.548	1.606	1.591
R(MO)	1.827	2.016	1.987
$R(OH_f)$	0.965	0.965	0.966
$\varphi(H_aMO)$	173.1	140.7	154.3
$\varphi(MOH_f)$	108.4	103.8	105.2
$\delta(H_aMOH_f)$	126.1	79.3	89.6
E_e	-1595.956516	-203.356561	-195.293778
	TS (Ni)	**TS (Pd)**	**TS (Pt)**
R(MO)	1.987	2.196	2.234
$R(OH_f)$	0.971	0.968	0.969
$R(MH_b)$	1.503	1.523	1.577
$R(OH_b)$	1.420	1.545	1.371
$\varphi(MOH_f)$	101.5	97.5	94.0
$\varphi(H_bOH_f)$	98.7	98.0	100.4
E_e	-1595.868981	-203.314125	-195.233992

Table S6. Optimal geometries (distances in Å, angles in degrees), equilibrium energies E_e and energies E_{vert} at the $HMOH^-$ (^2A) optimal geometry (in a.u.) for the lowest singlet (^1A) and triplet (^3A) electronic states of HMOH, M = Ni, Pd, Pt, at the CCSD(T)/ATZ level of theory. The notation of the atoms is given in Figure S7(b).

Species	**HNiOH**	**HPdOH**	**HPtOH**
	^{1}A	**^{1}A**	**^{1}A**
$R(H_aM)$	1.438	1.499	1.512
R(MO)	1.715	1.911	1.886
$R(OH_f)$	0.967	0.966	0.969
$\varphi(H_aMO)$	102.8	90.8	103.1
$\varphi(MOH_f)$	110.5	108.3	106.3
$\delta(H_aMOH_f)$	66.0	50.9	73.9
E_e	-1595.876650	-203.300246	-195.222917
E_{vert}	-1595.844744	-203.269537	-195.183237
	^{3}A	**^{3}A**	**^{3}A**
$R(H_aM)$	1.537	1.579	1.577
R(MO)	1.763	1.917	1.929
$R(OH_f)$	0.960	0.965	0.964
$\varphi(H_aMO)$	164.1	142.5	147.9
$\varphi(MOH_f)$	122.2	114.3	116.7
$\delta(H_aMOH_f)$	106.1	81.8	84.7
E_e	-1595.892995	-203.262897	-195.185552
E_{vert}	-1595.890195	-203.259429	-195.182886

Table S7. Harmonic frequencies ω_i (cm^{-1}) of the lowest energy structures of $XMOX^-$, $M^-(X_2O)$, and their interconversion (transition) structure TS.

$HMOH^-$			**TS**			**$M^-(H_2O)$**		
				X = H				
M = Ni	**M = Pd**	**M = Pt**	**M = Ni**	**M = Pd**	**M = Pt**	**M = Ni**	**M = Pd**	**M = Pt**
420	415	480	1168 *i*	906 *i*	1417 *i*	108	95	102
450	768	573	345	323	270	232	71	128
591	1252	820	469	465	566	542	163	338
659	1795	1075	1074	811	723	1650	1680	1692
1740	2931	2168	1852	1960	1702	3477	3764	3355
3771	4504	3789	3672	3737	3661	3832	3982	3848
				X = D				
M = Ni	**M = Pd**	**M = Pt**	**M = Ni**	**M = Pd**	**M = Pt**	**M = Ni**	**M = Pd**	**M = Pt**
307	374	364	847 *i*	654 *i*	1018 *i*	76	67	72
336	568	517	314	313	257	164	68	121
478	991	631	367	341	408	383	116	243
582	1294	770	776	590	542	1167	1229	1237
1244	2089	1537	1332	1393	1208	2459	2729	2437
2743	3280	2759	2674	2719	2667	2709	2902	2800

Table S8. Activation energy (eV) from the $M^-(X_2O)$ local minimum to the $XMOX^-$ global minimum.

	M=Ni	**M=Pd**	**M=Pt**
E_a	1.219	1.046	1.013
	E_a (ZPE-corrected)		
X = H	0.996	0.837	0.768
X = D	1.074	0.897	0.837
	E_a (ZPE and SO-corrected)		
X = H	1.038	0.780	1.011
X = D	1.116	0.840	1.080

Activation energy: E_a(ZPE-corrected) = E_a + ZPE(TS) – ZPE[$M^-(X_2O)$].

ZPE = ½ $\sum\omega_i$. Imaginary frequencies treated as negative.

Table S9. Optimal geometries (distances in Å, angles in degrees) and equilibrium energies E_e for the lowest doublet ($^2B_1$) electronic state of H_2MO^-, M = Ni, Pd, Pt, at the CCSD(T)/ATZ level of theory. The notation of the atoms is given in Figure S7.

	H_2NiO^-	**H_2PdO^-**	**H_2PtO^-**
R(MO)	1.665	1.932	1.855
R(H_1M)	1.511	1.605	1.566
R(H_2M)	1.511	1.605	1.566
φ(H_1MO)	147.1	162.8	149.0
φ(H_2MO)	147.1	162.8	149.0
δ(H_1MOH_2)	180.0	180.0	180.0
E_e	-1595.889585	-203.315758	-195.270812
	TS_1 (Ni)	**TS_1 (Pd)**	**TS_1 (Pt)**
R(MO)	1.673	1.923	1.918
R(MH_f)	1.577	1.650	1.639
R(MH_b)	1.460	1.538	1.564
R(OH_b)	1.762	1.565	1.504
φ(H_fMH_b)	117.2	123.4	128.9
δ(H_fMH_bO)	180.0	180.0	180.0
E_e	-1595.884068	-203.277834	-195.226317

Table S10. Energies E_{vert} at the H_2MO^- ($^2B_1$) optimal geometry (in a.u.) for the lowest triplet ($^3B_1$) and singlet ($^1A_1$) electronic states of H_2MO, M = Ni, Pd, Pt, at the CCSD(T)/ATZ level of theory.

	Ni	**Pd**	**Pt**
		E_e	
H_2MO^- ($^2B_1$)	-1595.889585	-203.3157580	-195.2708120
H_2MO ($^3B_1$)	-1595.789148	-203.2242823	-195.1439057
H_2MO ($^1A_1$)	-1595.800836	-203.1981065	-195.1457906
		E_{vert}	
H_2MO ($^3B_1$)	2.75	2.49	3.45
H_2MO ($^1A_1$)	2.43	3.20	3.40

Table S11. Equilibrium energies E_e (a.u.), zero-point correction energies ZPE (kcal/mol), and energy difference between the lowest electronic state before and after the spin-orbit coupling SO (cm^{-1}).

Species	E_e	ZPE	E_e + ZPE	SO	E_e + ZPE + SO
			CCSD(T)/ATZ-PP		
H_2	-1.172636	6.29	-1.162618	0.0	-1.162618
H_2O	-76.342326	13.40	-76.320984	0.0	-76.320984
Pt^-	-118.908065	0.00	-118.908065	-3852.9	-118.925620
PtO^-	-194.034414	1.17	-194.032552	-2123.3	-194.042227
$Pt^- + H_2O$	-195.250391	13.40	-195.229049	-3852.9	-195.246605
$Pt^-(H_2O)$	-195.271214	13.68	-195.249434	-3655.5	-195.266090
TS_1	-195.233992	7.87	-195.221459	-1644.1	-195.228950
$HPtOH^-$	-195.293778	10.48	-195.277095	-3204.6	-195.291696
TS_2	-195.226317	6.14	-195.216544	-612.3	-195.219334
H_2PtO^-	-195.270812	9.49	-195.255693	-542.4	-195.258164
$H_2 + PtO^-$	-195.207049	19.69	-195.195170	0.0	-195.204844
Pd^-	-126.991696	0.00	-126.991696	0.0	-126.991696
PdO^-	-202.096863	0.92	-202.095398	-555.7	-202.097930
$Pd^- + H_2O$	-203.334022	13.40	-203.312681	0.0	-203.312681
$Pd^-(H_2O)$	-203.352567	13.95	-203.330358	214.0	-203.329383
TS_1	-203.314125	9.13	-203.299576	-123.1	-203.300137
$HPdOH^-$	-203.356561	11.02	-203.339018	-624.9	-203.341865
TS_2	-203.277834	5.65	-203.268841	-90.2	-203.269252
H_2PdO^-	-203.315754	9.32	-203.300910	-17.5	-203.300989
$H_2 + PdO^-$	-203.269499	7.21	-203.258015	-555.7	-203.260547
			CCSD(T)/ATZ-DK		
H_2	-1.172645	6.29	-1.162627	0.0	-1.162627
H_2O	-76.390761	13.39	-76.369431	0.0	-76.369431
Ni^-	-1519.505897	0.00	-1519.505897	-589.9	-1519.508585
NiO^-	-1594.682179	1.18	-1594.680306	-478.1	-1594.682485
$Ni^- + H_2O$	-1595.896658	13.39	-1595.875328	-589.9	-1595.878015
$Ni^-(H_2O)$	-1595.913764	14.07	-1595.891360	-528.3	-1595.893768
TS_1	-1595.868981	8.93	-1595.854765	-190.3	-1595.855632
$HNiOH^-$	-1595.956516	10.91	-1595.939143	-653.0	-1595.942118
TS_2	-1595.884068	6.59	-1595.873573	-106.9	-1595.874060
H_2NiO^-	-1595.889585	9.11	-1595.875072	-149.3	-1595.875752
$H_2 + NiO^-$	-1595.854824	7.47	-1595.842933	-478.1	-1595.845112

Table S12. Coefficients of the largest configuration in the CI expansion of all of the states considered in this work.

Species	M = Ni	M = Pd	M = Pt
M (^{3}D)	0.96	0.97	0.98
M^- (^{2}D or ^{2}S) [a]	0.97	0.98	0.99
HMOH (^{3}A)	0.95	0.94	0.94
HMOH (^{1}A)	0.85	0.91	0.84
$HMOH^-$ (^{2}A)	0.90	0.92	0.92
H_2MO ($^1A_1$)	0.81	0.82	0.83
H_2MO ($^3B_1$)	0.88	0.92	0.94
H_2MO^- ($^2B_1$)	0.90	0.97	0.96

[a] The ^{2}S corresponds to Pd.

References

(1) Werner, H. J. Matrix-formulated direct multiconfiguration self-consistent field and multiconfiguration reference configuration-interaction methods. *Adv. Chem. Phys.* **1987**, *59*, 1-62.

(2) Werner, H. J.; Reinsch, E. A. The self-consistent electron pairs method for multiconfiguration reference state functions. *J. Chem. Phys.* **1982**, *76*, 3144-3156.

(3) Dunning, T. H. Gaussian basis sets for use in correlated molecular calculations. I. The atoms boron through neon and hydrogen. *J. Chem. Phys.* **1989**, *90*, 1007-1023.

(4) Kendall, R. A.; Dunning, T. H.; Harrison, R. J. Electron affinities of the first - row atoms revisited. Systematic basis sets and wave functions. *J. Chem. Phys.* **1992**, *96*, 6796-6806.

(5) Figgen, D.; Peterson, K. A.; Dolg, M.; Stoll, H. Energy-consistent pseudopotentials and correlation consistent basis sets for the 5d elements Hf-Pt. *J. Chem. Phys.* **2009**, *130*, 164108.

(6) Peterson, K. A.; Figgen, D.; Stoll, H. Energy-consistent relativistic pseudopotentials and correlation consistent basis sets for the 4d elements Y-Pd. *J. Chem. Phys.* **2007**, *126*, 124101.

(7) Douglas, M.; Kroll, N. M. Quantum electrodynamical corrections to the fine structure of helium. *Ann. Phys.* **1974**, *82*, 89-155.

(8) Hess, B. A. Applicability of the no-pair equation with free-particle projection operators to atomic and molecular structure calculations. *Phys. Rev. A* **1985**, *32*, 756-763.

(9) Jansen, G.; Hess, B. A. Revision of the Douglas-Kroll transformation. *Phys. Rev. A* **1989**, *39*, 6016-6017.

(10) MOLPRO is a package of ab initio programs written by H.-J. Werner, P. J. Knowles, G. Knizia, F. R. Manby, M. Schütz, P. Celani, W. Györffy, D. Kats, T. Korona, R. Lindh, A. Mitrushenkov, G. Rauhut, K. R. Shamasundar, T. B. Adler, R. D. Amos, A. Bernhardsson, A. Berning, D. L. Cooper, M. J. O. Deegan, A. J. Dobbyn, F. Eckert, E. Goll, C. Hampel, A. Hesselmann, G. Hetzer, T. Hrenar, G. Jansen, C. Köppl, Y. Liu, A. W. Lloyd, R. A. Mata, A. J. May, S. J. McNicholas, W. Meyer, M. E. Mura, A. Nicklaß, D. P. O'Neill, P. Palmieri, D. Peng, K. Pflüger, R. Pitzer, M. Reiher, T. Shiozaki, H. Stoll, A. J. Stone, R. Tarroni, T. Thorsteinsson, M. Wang, see http://www.molpro.net

(11) Scheer, M.; Brodie, C. A.; Bilodeau, R. C.; Haugen, H. K. Laser spectroscopic measurements of binding energies and fine-structure splittings of Co^-, Ni^-, Rh^-, and Pd^-. *Phys. Rev. A* **1998**, *58*, 2051-2062.

(12) Bilodeau, R. C.; Scheer, M.; Haugen, H. K.; Brooks, R. L. Near-threshold laser spectroscopy of iridium and platinum negative ions: Electron affinities and the threshold law. *Phys. Rev. A* **1999**, *61*, 012505.

(13) Peppernick, S. J.; Dasitha Gunaratne, K. D.; Castleman Jr., A. W. Superatom spectroscopy and the electronic state correlation between elements and isoelectronic molecular counterparts. *Proc. Natl. Acad. Sci.* **2010**, *107*, 975-980.

(14) E. A. Coutsias, C. Seok, K. A. Dill, Using quaternions to calculate RMSD. *J. Comput. Chem.* **2004**, *25*, 1849-1857.